TOWARD VERIFICATION AND VALIDATION OF THE MILANI IMAGE PROCESSING PIPELINE IN THE HARDWARE-IN-THE-LOOP TESTBENCH TINYV3RSE

F. Piccolo*, M. Pugliatti*, P. Panicucci†, F. Topputo‡

Verification and validation is an essential step for image processing and vision-based navigation algorithms. Typically these algorithms are designed mainly with synthetic images, which implies a urgent need to study their behaviour under realistic environmental conditions. To achieve this task, DART Lab has designed the hardware-in-the-loop testbench TinyV3RSE, which can be used both to support fundamental research and to increase the maturity of mission-specific algorithms. Among its projects, DART Lab is responsible for the mission analysis and the GNC subsystem of Milani, one of the two CubeSats of ESA's Hera mission. A crucial component of its semi-autonomous vision-based GNC subsystem is the image processing, which, to this date, has been designed and tested only with synthetic images. In this work the weighted center of brightness algorithm, an essential part of Milani's image processing, is tested using TinyV3RSE. In particular, the robustness of the algorithm to challenging geometrical conditions, different exposure times, and blur levels is investigated. The results allowed to prove the robustness of the algorithm and to gather insight into the effect of camera hardware on the image processing software: a preliminary but essential step towards the full validation and verification of Milani's image processing.

INTRODUCTION

Vision-based navigation (VBN) requires extensive verification and validation efforts not only to ensure the fulfillment of the algorithms' requirements in all the operative scenarios, but also to study the algorithm's limits and parameter-dependent sensitivities. The validation of VBN algorithms requires high-fidelity images which take into account environmental errors, such as spikes or stray-light, as much as sensor errors, such as rolling shutter effect or electronics-induced errors. To this aim, two approaches are usually employed: high-fidelity rendering simulations or hardware-in-the-loop (HIL) testing. High-fidelity rendering engines, such as ESA's PANGU[1] or Airbus Defence & Space's SurRender,[2] enable to simulate at software level the images received from the on board computer. On the contrary, HIL test-benches rely on the use of the manufactured sensor - or an engineering model - in a laboratory space-representative environment.

In the last decades, HIL testing has been widely employed to test image processing (IP) algorithms in space-representative conditions using dedicated facilities. Historically, optical test benches have been used to test and characterize star trackers,[3–6] while dynamic test benches have been employed

---

*PhD Student, Department of Aerospace Science and Technology, Politecnico di Milano, felice.piccolo@polimi.it, mattia.pugliatti@polimi.it

†Postdoctoral Research Fellow, Department of Aerospace Science and Technology, Politecnico di Milano, paolo.panicucci@polimi.it

‡Full professor, Department of Aerospace Science and Technology, Politecnico di Milano, francesco.topputo@polimi.it

for close proximity operations and landing scenarios.[7–10]

On the one hand, optical test benches usually consist of a high-resolution screen that stimulates an optical device in a dark room to reproduce deep sky conditions. A series of lenses, often including a collimator, is interposed between the stimulating screen and the optical device to reduce the facility mass and size. This implies that these facilities are usually quite compact. Moreover, the absence of moving mechanisms reduces the calibration effort and ensure design simplicity. On the other hand, dynamic test benches rely on an optical device which is mounted on a robotic arm. The latter moves about a target mock-up or surface analog to simulate the spacecraft's VBN. This concept enables to reproduce as closely as possible the real operating environment, but such facilities are complex, expensive, and bulky. An intermediate approach consists in using an optical test bench while simulating the close-proximity dynamics in a dedicated server. This reduces infrastructure costs while ensuring representative camera errors.

This latter approach drove the design of the DART (Deep-space Astrodynamics Research & Technology) Vision-Based Navigation test-bench TinyV3RSE (Tiny Versatile 3D Reality Simulation Environment), which has been devised not only to promote fundamental research on spacecraft autonomy[11] but also to support the validation of the IP and VBN algorithms DART is designing for upcoming space missions, such as Milani,[12] LUMIO[13] and M-ARGO.[14]

In this work, the core algorithm of Milani's IP pipeline is tested and validated in a static framework, without simulating the rest of the GNC subsystem. First, images are rendered by changing important parameters such as the relative positions of D1, D2 and the spacecraft, and the asteroids' shape. This provides a vast dataset where a wide set of possible geometrical configurations and uncertain-before-arrival asteroids parameters are dispersed. Furthermore, datasets generated from the nominal mission trajectory are also considered. Second, images are acquired in TinyV3RSE with different camera settings, namely exposure time and blur, to understand whether the algorithm can operate in degraded situations. An example of image acquisition is presented in Figure 1, where a synthetic image is compared with the one taken employing TinyV3RSE.
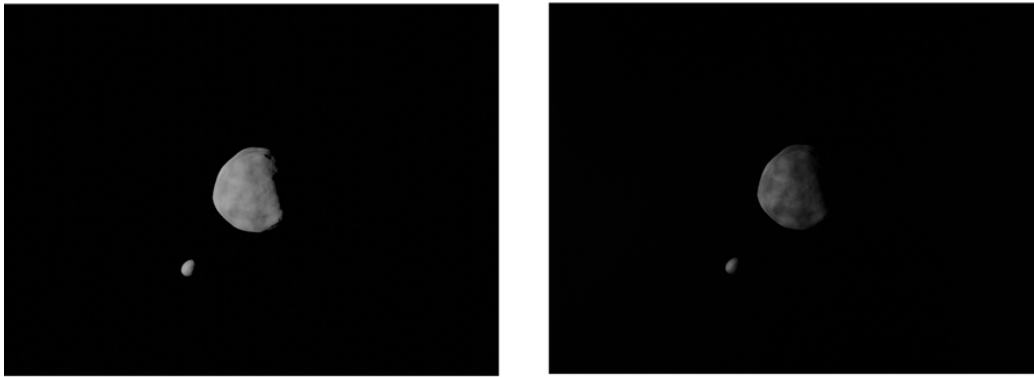

Figure 1: Rendered image of Dydimos compared with the same image as taken during an HIL validation test.

Overall, the scope and achievements illustrated in this paper can be better understood by framing it properly amongst other activities performed by the DART team. Indeed, two works can be identified as pillars of this study. The first one is the design and calibration procedure of the TinyV3RSE facility, illustrated in Reference 15. The second one is the design of the Milani IP software, which

is discussed at length in Reference 16. For this reason, specific elements pertaining the IP of Milani and the design of the TinV3RSE facily are not discussed here at length but can be consulted by the interested reader in the aforementioned works.

The remainder of the paper is organized as follows. First, a detailed description of the TinyV3RSE facility is given, followed up by a brief discussion about the Milani mission and its IP algorithm. Then, the methodology followed to define the test cases is described and the results of the different test cases are discussed.

TINYV3RSE

TinyV3RSE[15] is the vision-based navigation test bench designed and built at DART. TinyV3RSE is composed of three main elements: a high-resolution stimulating screen, an optical device, and a collimating lens which ensures that the light coming from the screen and entering the camera is simulated as coming from infinity (or from a very high distance). These three elements are mounted on dedicated optical stages and placed on an optical breadboard within a black enclosure. The screen and the optical elements are shown in a CAD rendering in Figure 2 and in the top view of the TinyV3RSE facility in Figure 3. Although the design of TinyV3RSE is outside the scope of the present paper, the facility elements are described rapidly hereunder for the sake of completeness. The interested reader can refer to Reference 15 for further details. TinyV3RSE's hardware has the following characteristics:

1. The camera is a Balser acA1300-22gm (CS-Mount) 2 with a 12mm C Series Fixed Focal Length Lens. The camera resolution is 1280 pixels $\times$ 960 pixels with squared pixels of 3.75 μm $\times$ 3.75 μm.

2. The screen is a Galaxy S7 phone. it has a resolution of 2560 pixels $\times$ 1440 pixels with squared pixels of 44.1 μm $\times$ 44.1 μm.

3. The collimator is a $\varnothing$2" N-BK7 Plano-Convex lens with a focal length of 200 mm.

The hardware has been selected to cover with the camera field of view (FOV) the widest portion of the screen after collimation without encountering any vignetting effect.

Functional Workflow

In Figure 4 TinyV3RSE's functional workflow as used in the present study is outlined. To design IP and VBN algorithms, a simulated world is defined where the physical and geometrical characteristics of the spacecraft and of the celestial bodies under study are defined. By defining a convenient camera characteristics, the scene can be rendered according to the user needs by simply changing the geometrical configuration and the camera characteristics. This step is depicted in Figure 4 in the left part of the sketch where the mission camera generates the ideal mission image from the pose, i.e. position and orientation, defined by the mission needs. This is the general approach to design and assess preliminary performances of the IP and VBN algorithms. The other parts of Figure 4 depict the procedure needed to use TinyV3RSE. A screen camera is defined according to the mission camera characteristics and TinyV3RSE's screen properties to generate a screen image. This image must have the screen resolution to fit the screen when displayed while containing pieces of information consistent with the ideal mission image. When the image is projected on the screen, the camera is stimulated by the screen through the collimator and it captures the facility image. With
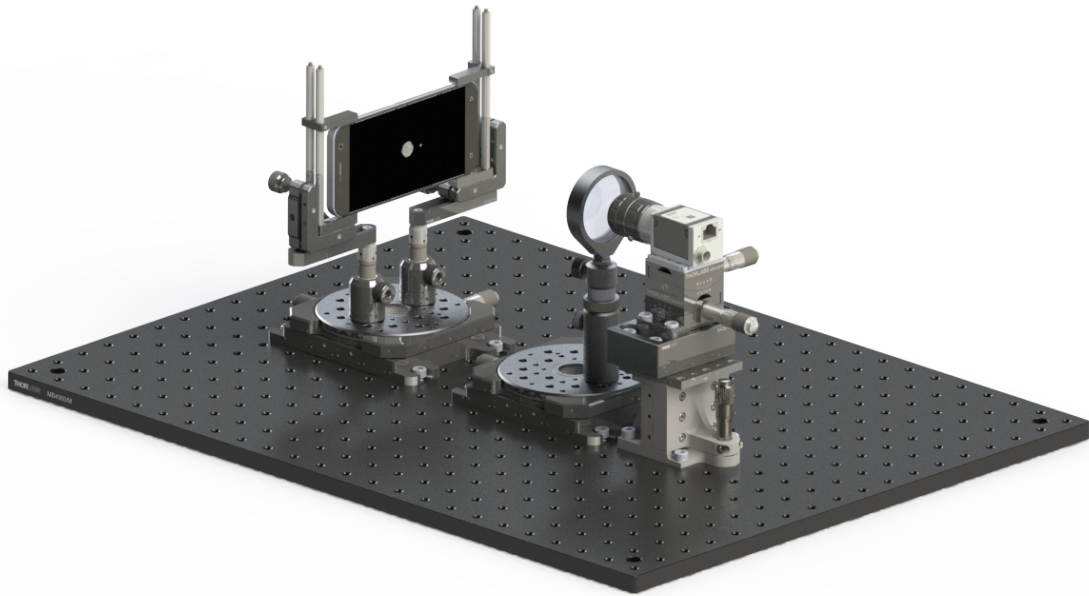
Figure 2: CAD model of TinyV3RSE
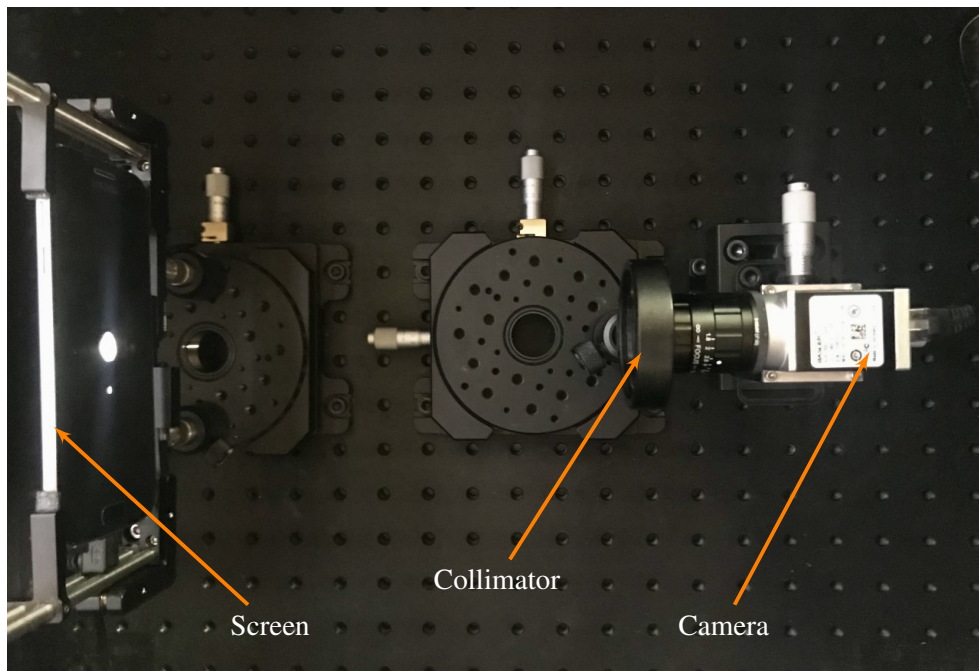

Collimator

Screen

Camera

Figure 3: Top view of the TinyV3RSE facility.

the proper settings and the proper calibration procedure, the facility image and the ideal mission image are geometrically equivalent, but photometrically different. The latter is due to several reasons. First, many rendering engines, e.g. Blender and POV-Ray, are not physics-based rendering software which implies that light is not not considered from radiometric perspective, but only from the geometrical one. Second, the screen is not radiometrically calibrated as no mapping has been determined between the pixel digital count and the screen pixel radiance as done for example in Reference 5.

Software Functionalities

TinyV3RSE's software functionalities ensure not only an easy-to-use interface to communicate with the hardware during simulations, but also a user-friendly program to calibrate the facility and estimate the camera point spread function (PSF). These functionalities are rapidly outlined hereunder and the interested reader can refer to Reference 15 for further details. The calibration is resolved in a sequential procedure which enables to estimate the camera intrinsic matrix, the calibration distortion model, and the camera-screen misalignment. This is of fundamental importance to have a facility image consistent geometrically with the ideal mission image. To give an example of the calibration performances, the estimated calibration model places 98% of the calibration points under the screen iFOV which is the angular size of the smallest point that can be displayed on the screen. An important step to be performed before using the facility is the characterization of the optical response of the camera in TinyV3RSE. TinyV3RSE's software include an algorithm to retrieve the best Gaussian fit of the PSF of the facility camera. This important functionality provides the operator a way to quantify the camera blur and study the algorithm under different blur conditions.
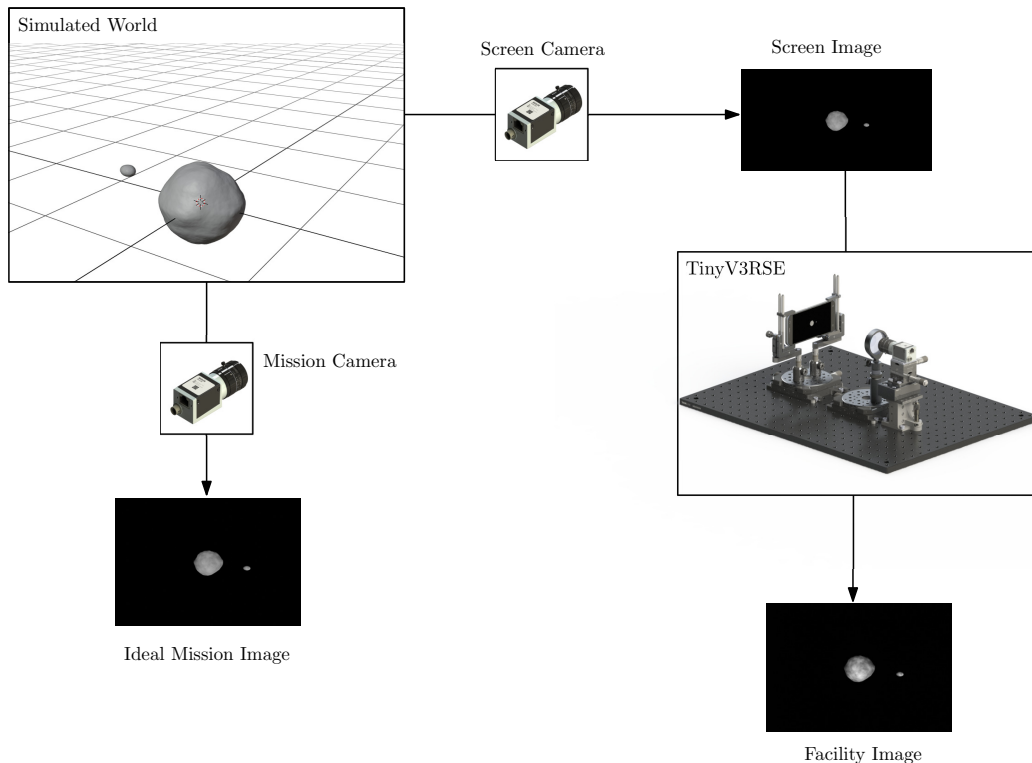

Figure 4: Functional workflow in TinyV3RSE

5

MILANI'S IMAGE PROCESSING

Milani is a 6U CubeSat, part of ESA's Hera mission,[17] which will visit and characterize the Didymos binary system. The primary and secondary bodies of the system are called Didymos and Dimorphos, hereafter also referred to as D1 and D2, respectively. After release from the Hera mothership, Milani will focus on its scientific objectives, namely the characterization of Didymos' asteroids and their surrounding environment. Milani will also demonstrate CubeSat technologies in deep space, including Inter-Satellite Link (ISL) for communication with Hera and autonomous optical navigation (OpNav). Therefore, Milani is a semi-autonomous spacecraft that combines innovative IP and autonomous navigation components with traditional guidance and control approaches. Milani's mission profile is characterized by two main phases: a far range phase (FRP) lasting 21 days and a close range phase (CRP) lasting 28 days. The nominal trajectory of the spacecraft during these phases is illustrated in Figure 5. The reference frame employed is the so-called 'DidymosEquatorialSunSouth'. It is centered in the Didymos system barycenter, and it has its x-y plane on the equator of D1, with the x axis aligned to the projection of the Sun vector on the equator, while the z axis is aligned to the south pole of Didymos. The FRP exhibits symmetrical arcs that develop within 8-14 km from the main body. The CRP, instead, is characterized by asymmetrical arcs within 2-11 km from D1.[18]
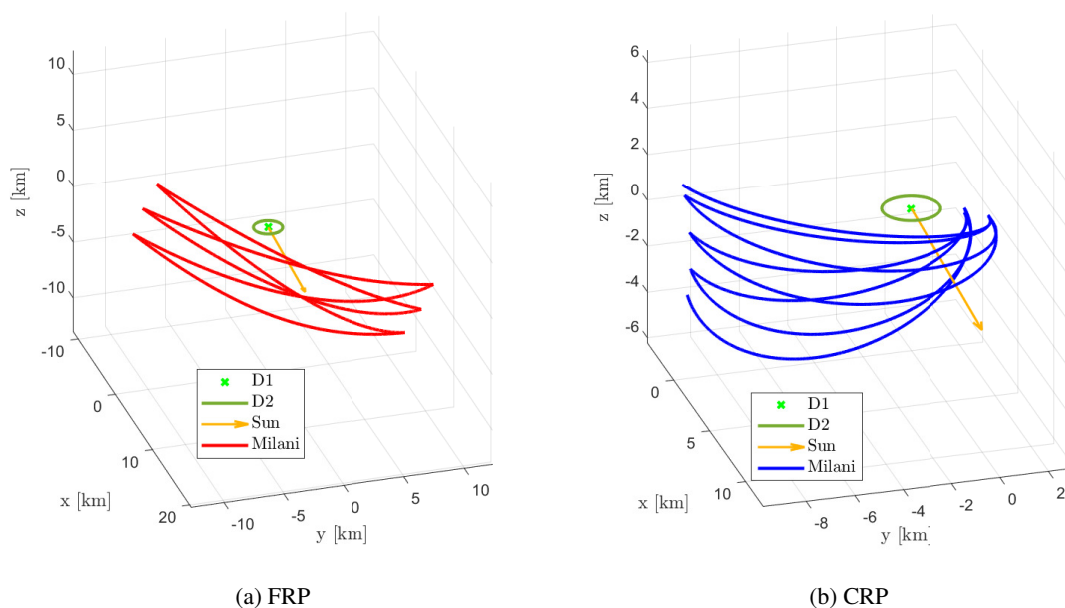

(a) FRP   (b) CRP

Figure 5: Trajectory of the spacecraft during the two main mission phases.

Milani's autonomous navigation mostly relies on observables produced by its IP algorithm. Thus, the latter needs to provide reliable data about D1 for navigation, but at the same time has to be able to distinguish D2 in the image to provide the navigation filter with reliable observables and to perform accurate pointing. Indeed, D1 is the largest, most visible, and regular body, which makes it the most suited for navigation purposes. Nevertheless, D2 is the main scientific target of the mission, so the spacecraft must be able to precisely point at it. To fulfill these requirements, the IP pipeline

is divided in two main blocks: the 'Blobs Characterization' and the 'Observables Extraction'. The former distinguishes D1 from D2 in the images and generates low-level observables by applying a simple blob analysis, while the latter refines these observables to extract geometrical quantities of interest that are used by the GNC, like the Center of Figure (CoF) of D1 and D2, the range from D1, the phase angle etc. These quantities can be produced according to three different algorithms: COB (Center Of Brightness), WCOB (Weighted Center Of Brightness) and SSWCOB (Sun Sensor Weighted Center Of Brightness). This work is focused on the WCOB method, which is a data-driven method based on designer-defined functions whose fitting coefficients are found employing a global dataset of images of the Didymos system.

The algorithm works as follows. First, the phase angle and range from D1 are estimated, starting from the results of the blob analysis. In particular, the PA is estimated by a data-driven function Ψ using the eccentricity e of the blob of pixels associated to D1. The range, instead, is estimated using the following equation:

$$\rho = \frac{R_{\mathrm{D1}}}{\tan\left(\frac{\delta \cdot \Omega}{2}\right)} \tag{1}$$

where R_{D1} is the radius of D1, δ is the semimajor axis of the ellipse fitted to the largest blob of pixels in the image and Ω is the istantaneous field of view (IFOV) of the camera. Second, the CoF estimation is computed using the following equation:

$$\begin{bmatrix} \mathrm{CoF}_x \\ \mathrm{CoF}_y \end{bmatrix} = \begin{bmatrix} \mathrm{CoB}_x \\ \mathrm{CoB}_y \end{bmatrix} + \omega \cdot \mathrm{M}(\Psi(e), \delta) \cdot \begin{bmatrix} \cos(\Phi) \\ \sin(\Phi) \end{bmatrix} \tag{2}$$

where CoB_x and CoB_y are the components of the CoB computed by the blob analysis, ω is a weighting parameter, and M and Φ are data-driven functions which estimate respectively the magnitude and orientation for the correction term. To compute the orientation Φ, a Sobel filter is applied on the image to distinguish between the edge and the terminator region of D1. For further details, the interested reader is directed to Reference 16 for an exhaustive explanation of the IP software of Milani and the WCOB algorithm and to Reference 19 for a performance comparison between Equation 2 and machine learning options.

Since the WCOB algorithm is trained with a set of synthetic images of the Didymos system, testing it using images acquired with the TinyV3RSE facility is a key step towards the V&V of the IP algorithm.

METHODOLOGY

As described in the previous section, the first step needed to run the WCOB algorithm is the training of its data-driven functions. For this purpose, a dataset of synthetic images was generated by acquiring the simulated world with an ideal mission camera. In this work, this camera is defined with the same characteristics as the facility one. Since Milani will move on hyperbolic arcs that always stay above the illuminated side of D1, the algorithm has been trained by considering an azimuth between ± 95 deg and an elevation between ± 45 deg in the DidymosEquatorialSunSouth frame, and a working range of 4 to 14 km from the main body. Then, to test the WCOB in a variety of conditions, datasets composed of different geometrical configurations have been generated, both randomly and considering mission-specific scenarios. An overview of the datasets is given in Table 1, while a graphical representation is provided in Figure 6. In all cases, the camera is assumed to be pointing exactly towards the CoM of the main body.

DS0 and DS1 are generic datasets, representative of the possible conditions that can be encountered

Table 1: Geometric datasets description.

Dataset	N. of images	Description
DS0	10000	D1, D2 and the spacecraft's positions are set randomly. Used for training the WCOB algorithm.
DS1	5000	D1, D2 and the spacecraft's positions are set randomly, but are different from those contained in DS0.
DS2	2840	Challenging geometrical conditions: D2 is overlapping partially or totally with D1.
FRP	4032	Obtained by sampling the first two arcs of the FRP trajectory of Milani every 150 seconds.
CRP	4032	Obtained by sampling the first two arcs of the CRP trajectory of Milani every 150 seconds.
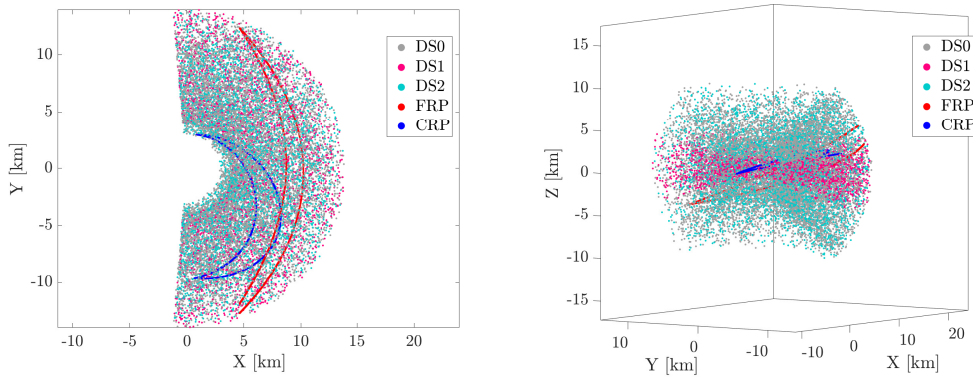
Figure 6: Point clouds corresponding to the different datasets.

within the IP design boundaries. The former is the one used for training, while the latter is employed for testing purposes. DS2 has been devised as a particularly challenging dataset, since the overlap of D2 over D1 tends to worsen the performance of the algorithm, especially when D2 is superimposed on the edge of D1. Two examples from this dataset are illustrated in Figure 7. Finally, FRP and CRP are employed to test the algorithm on a portion of the nominal mission trajectory. In these datasets, the only modification made to the trajectory is to slightly scale the range in order to compensate for the different FOV of the mission camera employed in this work with respect to Milani's navigation camera. More details about the latter can be found in Reference 16.

Starting from DS1, three additional datasets have been generated by changing the dimensions of the main body, D1. In the first one, the dimensions of the body along all directions have been reduced by 5%. In the second set, only the z direction of the body frame has been scaled by 5%, thus increasing the oblateness of the body. Finally, in the last set the oblateness has instead been reduced by scaling only the x and y directions of the body frame by 5%.

All the synthetic datasets, except DS0, have been acquired using TinyV3RSE. DS1 has been acquired with different camera settings to study the effect of the exposure time and of the blur on the
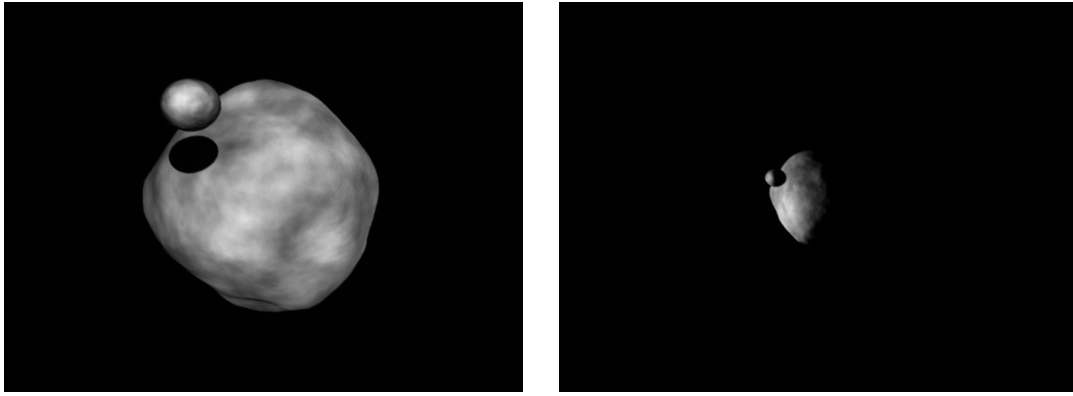
Figure 7: Facility images showing two cases of overlap of D2 on the edge of D1

WCOB performance. The exposure time has been set to span from highly under-exposed images to highly over-exposed ones. In particular, five values have been tested: 1 ms, 4 ms, 7 ms, 10 ms, and 50 ms. Furthermore, after fixing the exposure time, images with three levels of blur have been acquired, characterized by an increasingly wider PSF with σ_{blur} equal to 0.77, 1.47 and 2.60 pixel. A comparison of a facility image acquired with the different exposure times is given in Figure 8, while in Figure 9 images with the three different levels of blur are shown. The other datasets, instead, have been only acquired with low blur and with a fixed exposure time of 7 ms, that has been selected qualitatively to resemble realistic asteroid images.
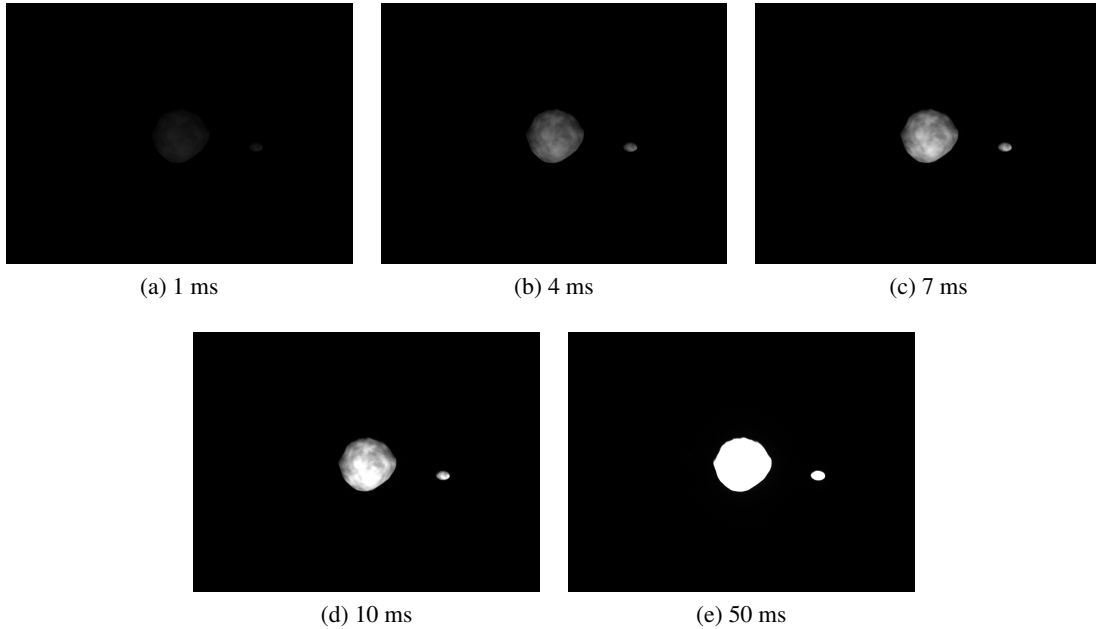

(a) 1 ms

(b) 4 ms

(c) 7 ms

(d) 10 ms

(e) 50 ms

Figure 8: Facility images with different exposure times.

To correctly evaluate the WCOB performance, images are taken from the facility camera and then corrected to compensate facility errors estimated during TinyV3RSE's calibration procedure. For each dataset, the algorithm is run on both the facility and the synthetic images. This allows to prop-
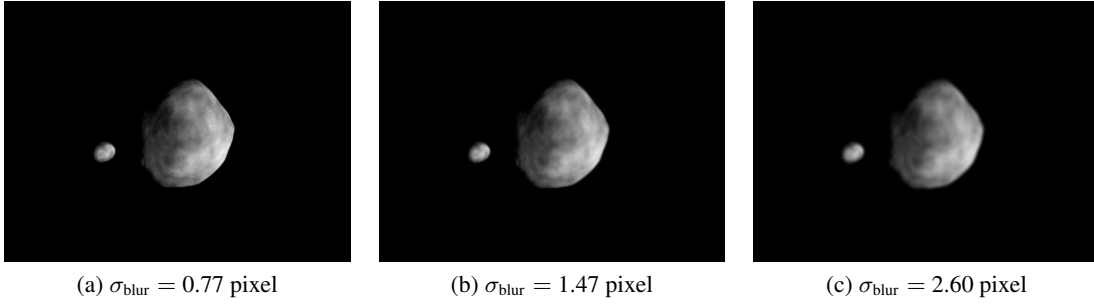
(a) $\sigma_{\text{blur}} = 0.77$ pixel   (b) $\sigma_{\text{blur}} = 1.47$ pixel   (c) $\sigma_{\text{blur}} = 2.60$ pixel

Figure 9: Facility images with different blur levels.

erly evaluate the impact of the hardware on its performance. Then, the error with respect to the true values of center of mass (CoM) coordinates, phase angle and range is also analyzed.

RESULTS

In this section the results obtained from the different test cases are reported and discussed. As stated previously, the output of the WCOB obtained from facility images is compared both with the truth values and with the ones obtained from running the algorithm on synthetic images. In particular, the estimate of the CoF of D1, phase angle and range, are considered. The error in the CoF estimate is the most interesting one, and it is analyzed by considering both the error in the x and y components and the error norm, computed as:

$$\varepsilon_{\text{n}} = \sqrt{\varepsilon_{\text{x}}^2 + \varepsilon_{\text{y}}^2} \tag{3}$$

where ε_{x} and ε_{y} are the errors in the x and y components in the image plane. The errors on the phase angle and range are indicated respectively as ε_{PA} and $\varepsilon_{\text{Range}}$. The difference between the errors obtained from facility images and the ones obtained from synthetic images, instead, is indicated by placing a Δ before the corresponding variable (e.g. $\Delta\varepsilon_{\text{x}}$ and $\Delta\varepsilon_{\text{y}}$).

The results for the different test cases are discussed in the following sections. At the end, table 2 gives a summary of the error statistics on all test cases.

Exposure time

The results of the tests conducted on DS1 with varying exposure time are presented in Figure 11. The box plots on the left represent the distribution of the error obtained by running the WCOB algorithm on facility images. On the right side, instead, the distribution of the difference between the estimation obtained from facility images and from synthetic ones is shown. It can be seen that for exposure times from 1 ms to 10 ms, the impact on the algorithm performance is minimal. However, as the exposure time increases, the performance on the facility images gets slightly closer to the one on the synthetic images. Indeed, the variability of the difference distributions reduces. The low impact of the exposure times can be explained by the binarization of the image, that is the first step of the image processing pipeline. Since in this work the algorithm is set to automatically select the binarization threshold using Otsu's method, the binarization step performs well even with very low or very high exposure times.

Furthermore, it can be noted that the x and y components of the CoF are generally estimated well, as the median of the error is close to 0, while a significant bias is visible for the phase angle and

range. This can be again explained by the binarization step: facility images show a higher intensity variability with respect to synthetic images, and therefore a higher binarization threshold is usually selected. As a result, more pixels are cut out during this step, resulting in a smaller blob of pixels associated to D1, as can be observed in Figure 10. Since the range and phase angle are estimated from the characteristics of this blob, this translates into biased errors. In particular, the range is determined from the blob's semimajor axis, therefore a smaller blob leads to an overestimation of the range. The phase angle, instead, is estimated from its eccentricity. Since the additional pixels that are cut out from the facility images are usually grouped around the terminator region of the asteroid, the eccentricity of the binarized blob tends to increase, resulting in a higher estimate of the phase angle. These effects can be appreciated in Figure 10, where the difference between a binarized facility and synthetic image is shown, together with the CoB of the two blobs and the fitted ellipses. The gray area is the one that is retained in the binarized synthetic image, but is discarded in the binarized facility image. This leads to a shift of the CoB (the blue/red dot) and to a different ellipse fit. The blue ellipse, obtained from the fit of the binarized facility image, is characterized by a smaller semimajor axis and a higher eccentricity with respect to the synthetic one, as described before. This leads to the overestimation of the range and phase angle.

An interesting case is the one with the 50 ms exposure time. In this case, the algorithm's performance improves significantly. This can be explained by the fact that the exposure time is so high that the image is composed mainly of saturated and black pixels, as seen in Figure 8. In contrast with the other cases, this makes the image binarization easier and helps better distinguish the edge of D1 from the terminator region. The combination of these effects is causing the binarized facility images to be very similar to the synthetic ones.
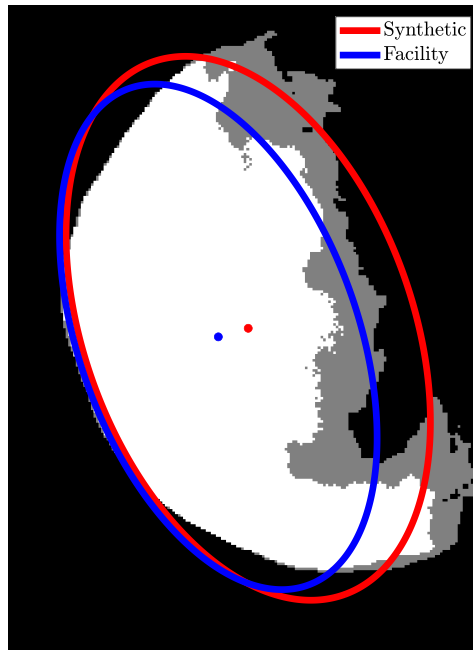

Figure 10: Comparison between the blobs of pixels obtained from the binarization of facility and synthetic images. The fitted ellipse and CoB resulting from the blob analysis are also shown.

Blur

The results for the different levels of blur are depicted in Figure 12. As for the previous section, box plots representing the estimation error and the difference between the results from the facility and synthetic images are shown for the variables of interest. Once again, the WCOB algorithm proves to be robust, since the impact of the increasing level of blur on its performance is minimal. Indeed, all variables show similar errors across the three test cases. The error on the x component of the CoF tends to spread more as the blur increases, as expected, since this is the direction that is most corrected by the WCOB method, that works better with low blur. On the other hand, the y component difference is lower at higher blur, even if it does not show a definite trend, and the same is seen for $\Delta\varepsilon_x$.

Shape

The box plots resulting from the analysis of the datasets with different body shapes are reported in Figure 13. As before, the error distribution is shown on the left, while on the right the difference between the performance of the algorithm on the facility images and the synthetic ones is presented. The ticks on the horizontal axis show which axes have been scaled with respect to the nominal shape model of D1. Considering the CoF, the performance of the WCOB improves when scaling all the body axes and the x-y axes. This can be explained by considering that for a smaller body the CoB will be closer to the CoM, which reduces the need for corrections. Indeed, when only the x-y axes of the body are scaled, the x component of the CoF estimation error is smaller, while the y component behaves similarly to the nominal case. Recall that, since the spacecraft elevation is limited between ± 45 deg, changes in the x and y axes of the body frame reflect mostly on the x direction of the image, while changes in the z axis of the body frame reflect mostly on the y direction of the image. Indeed, when scaling the z axis the performance in the x direction is worse than the nominal case, while the error on the y direction is smaller.
The phase angle performs best in the nominal case, and in general it shows less variability among the different cases. The main effect that can be observed is that the distribution spreads more when scaling the z axis. The range estimation, instead, is significantly impacted by the shape change. When all the axes are scaled the range is further overestimated, since the body appears smaller in the images. Furthermore, it can be observed that scaling the z axis instead of the x-y axes has the largest impact on the range estimation. This is mainly due to the fact that the range estimation is obtained from the semimajor axis of the ellipse fitted to the blob of pixels associated with D1. Since this semi-major axis is generally directed as the projection of the asteroid z axis on the image, scaling the z axis affects the most the range estimation.
Finally, from the plots on the right it can be seen that the difference between the estimates obtained from the facility images and the ones from the synthetic images show less variability with respect to the plots on the left. This is due to the fact that scaling the body dimensions has similar effects on both facility and synthetic images.

DS2

The performance of the IP algorithm on DS2 is shown in Figure 14. On the left side, the histograms show the estimation error of the algorithm when run on synthetic and facility images. On the right side, instead, the difference between the WCOB output on the facility images and the one on the synthetic images is shown. The histograms have been normalized to be representative of the Probability Density Function (PDF). Even for this challenging dataset, the CoF estimation performs

12

well. Indeed, the estimation error is distributed simmetrically around 0, both for the x and y directions. However, as expected, the error distribution obtained from facility images is more spread than the one obtained from synthetic images. As for the phase angle and range, as discussed before it can be noticed that the errors for the synthetic images are centered around 0, while the ones for the facility images show a bias.

Mission phases

The normalized histograms for the FRP and CRP datasets are shown in Figure 15 and Figure 16. As expected, the performance in these cases is significantly better than the one on DS2. The CoF estimation on the FRP dataset performs particularly well. Indeed, the total CoF error is mostly below 20 pixels. For the CRP case the CoF errors increase, which is expected since the spacecraft is closer to the system and thus D1 appears bigger in the images. Furthermore, in this case ε_x is slightly biased. This is due to the combination of the asymmetric CRP trajectory and the biased PA and range estimates. On the other hand, it is interesting to note that $\Delta\varepsilon_{\mathrm{Range}}$ is smaller for the CRP case. Indeed, as D1 is bigger in the images, the influence due to the different binarization on the semimajor axis of the pixel blob is smaller and the range estimated from the facility images is closer to the one obtained from synthetic images.

Table 2: Summary of the results. For each test case, the mean μ and standard deviation σ of the estimation errors are reported. The nomenclature used for the test cases is: $^{\mathrm{ScaledAxes}}\mathrm{Dataset}^{\sigma_{\mathrm{blur}}[\mathrm{px}]}_{\mathrm{ExpTime}\,[\mathrm{ms}]}$

| Test case	ε_x		ε_y		ε_n		ε_{PA}		$\varepsilon_{\mathrm{Range}}$	
	μ [px]	σ [px]	μ [px]	σ [px]	μ [px]	σ [px]	μ [°]	σ [°]	μ [m]	σ [m]
$DS1_1^{0.77}$	-1.13	20.3	-8.57	23.2	22.2	23.1	9.18	6.92	621.9	522.2
$DS1_4^{0.77}$	-1.06	19.1	-8.54	22.2	21.2	22.0	9.14	6.84	614.2	525.6
$DS1_7^{0.77}$	-1.34	18.8	-7.34	21.5	20.6	21.2	8.97	6.86	611.8	527.6
$DS1_{10}^{0.77}$	-1.03	18.1	-8.03	21.6	20.4	21.0	8.93	6.75	598.1	520.4
$DS1_{50}^{0.77}$	0.07	7.27	-4.85	13.0	10.7	11.4	-0.56	6.45	97.3	304.0
$DS1_7^{1.47}$	-0.08	17.6	-8.39	18.5	19.5	18.5	8.30	6.85	617.3	525.9
$DS1_7^{2.60}$	1.91	17.9	-8.74	18.3	20.0	18.4	7.18	6.90	651.1	532.9
$^{\mathrm{xyz}}DS1_7^{0.77}$	0.64	15.6	-4.86	18.1	17.5	17.0	8.94	6.86	1096	642.7
$^{\mathrm{xy}}DS1_7^{0.77}$	0.86	13.2	-5.36	20.5	17.4	17.9	10.4	7.13	751.1	539.1
$^{\mathrm{z}}DS1_7^{0.77}$	0.42	19.3	-4.17	17.2	19.6	17.4	8.39	8.62	894.9	672.4
$DS2_7^{0.77}$	-1.41	16.5	-6.19	22.2	20.5	19.7	9.95	6.64	471.6	495.2
$FRP_7^{0.77}$	-0.28	6.51	-2.59	7.68	8.78	5.56	9.82	6.44	604.0	483.2
$CRP_7^{0.77}$	5.15	8.23	-1.19	12.2	12.5	9.36	10.3	6.08	420.5	368.6
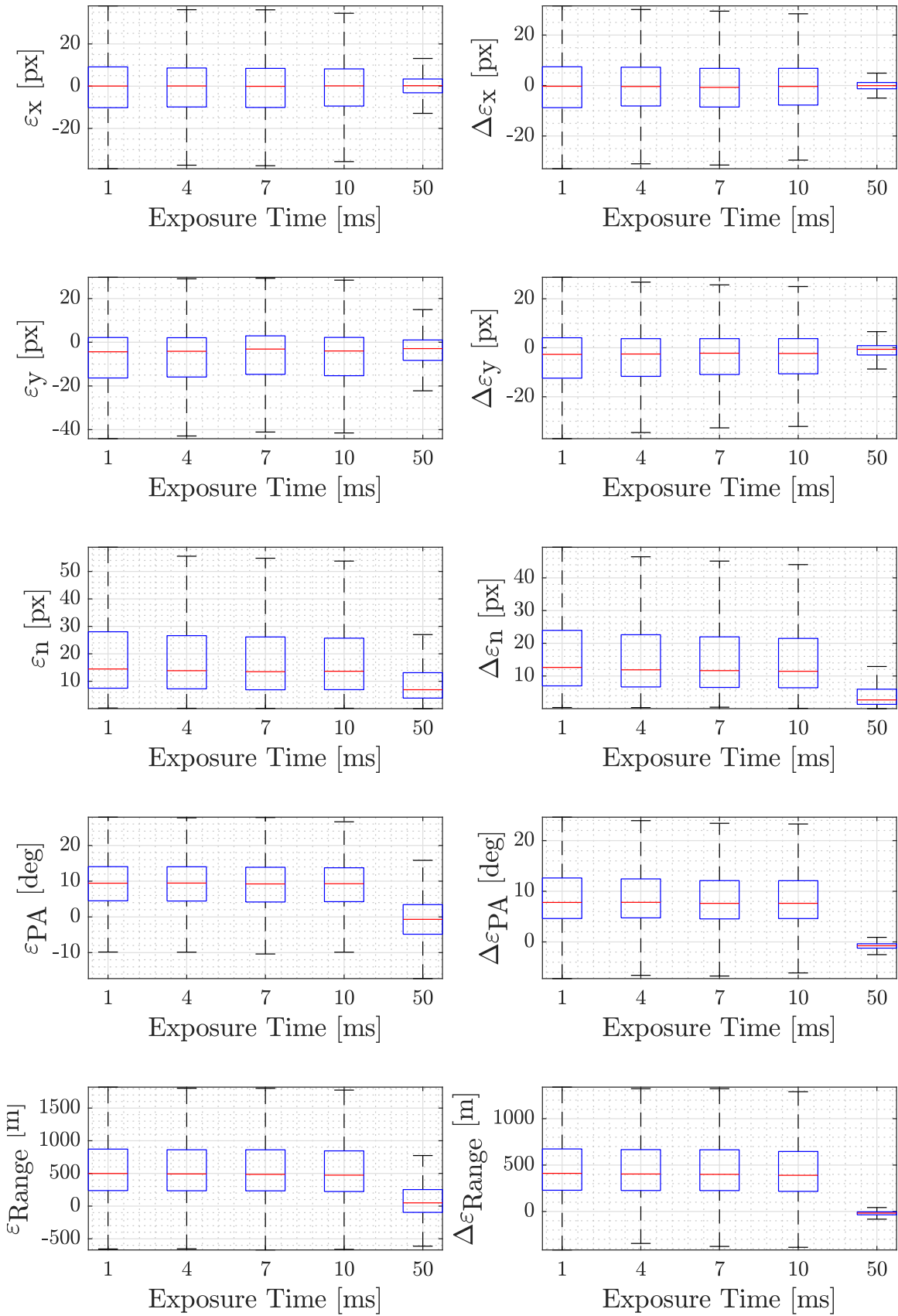
Figure 11: Results obtained from the DS1 dataset acquired with different exposure times. Left: Estimation errors statistics. Right: Difference between the IP output on facility images and synthetic images.
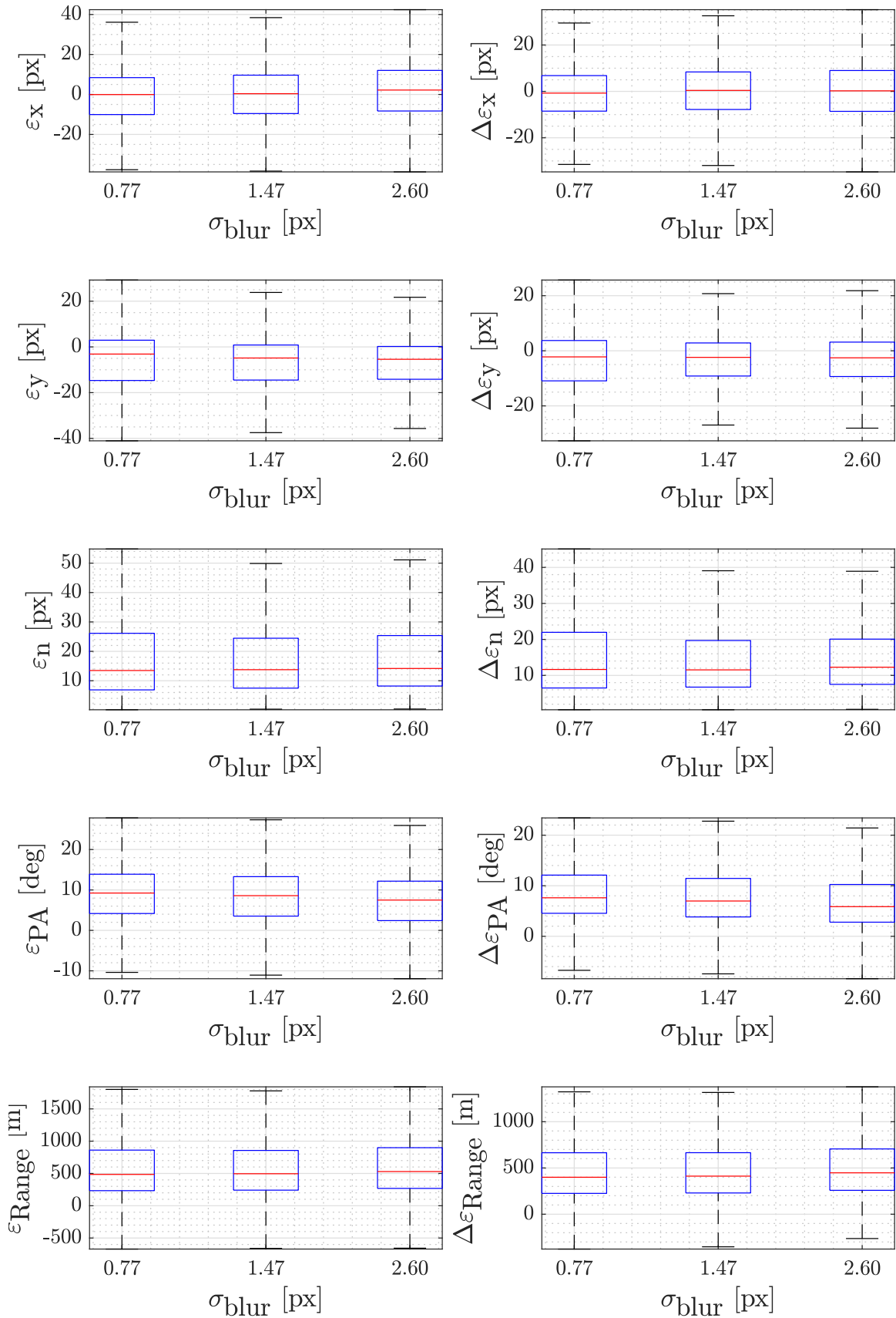
Figure 12: Results obtained from the DS1 dataset acquired with different levels of blur. Left: Estimation errors statistics. Right: Difference between the IP output on facility images and synthetic images.
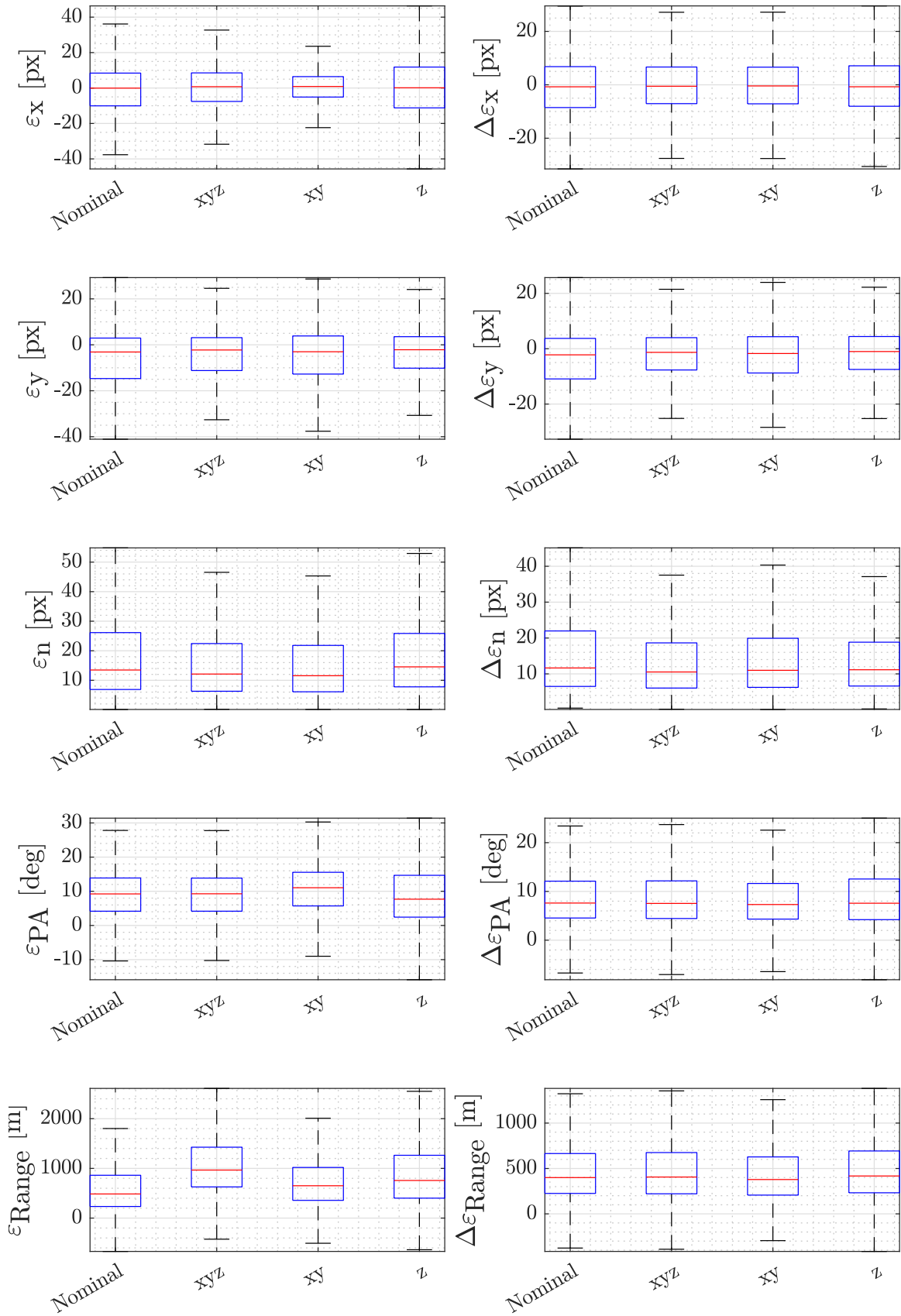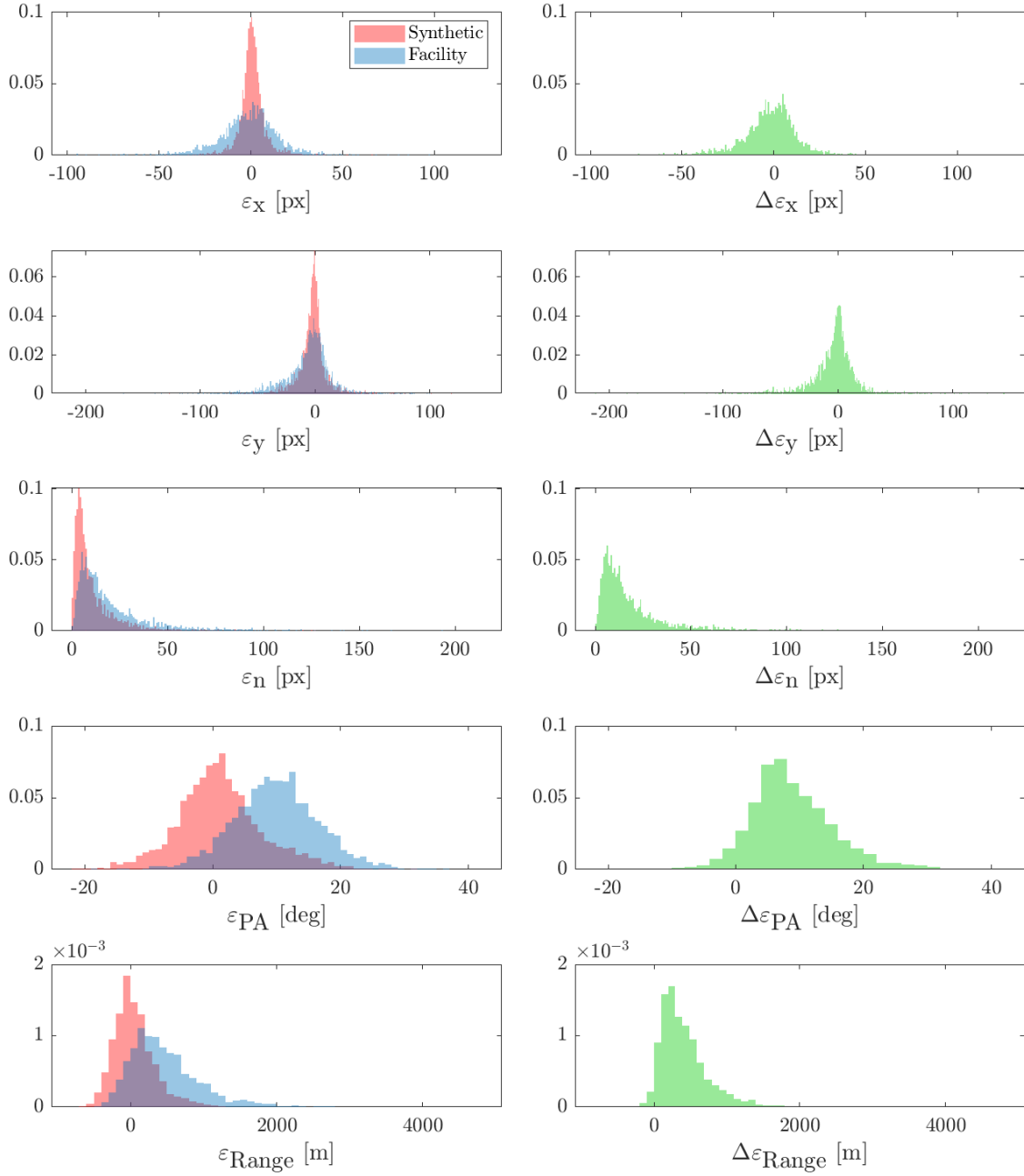
Figure 13: Results obtained from the DS1 dataset with different shapes of the main body. Left: Estimation errors statistics. Right: Difference between the IP output on facility images and synthetic images.

Figure 14: Results for the DS2 dataset, shown as normalized histograms. Left: Estimation errors statistics. Right: Difference between the IP output on facility images and synthetic images.
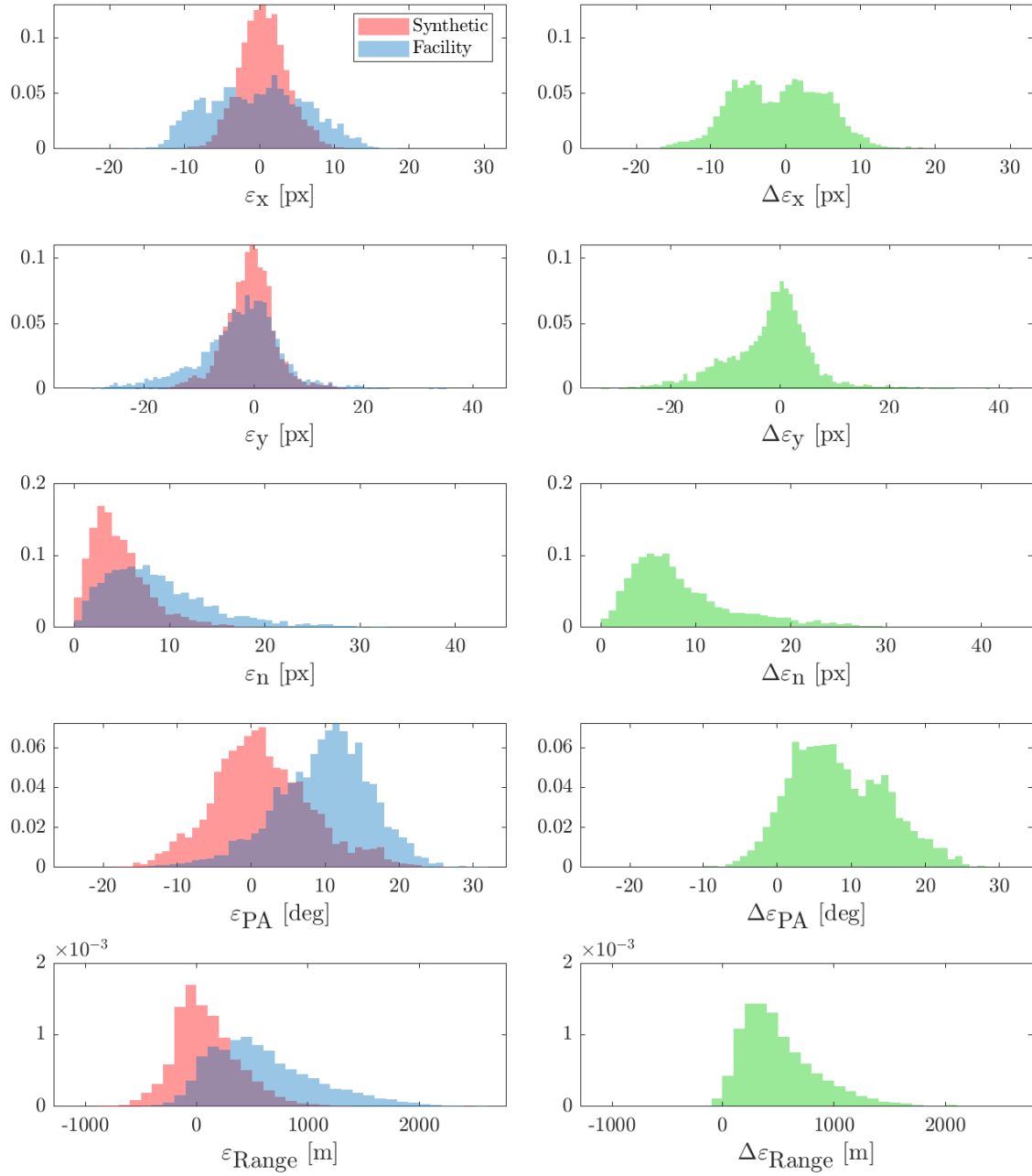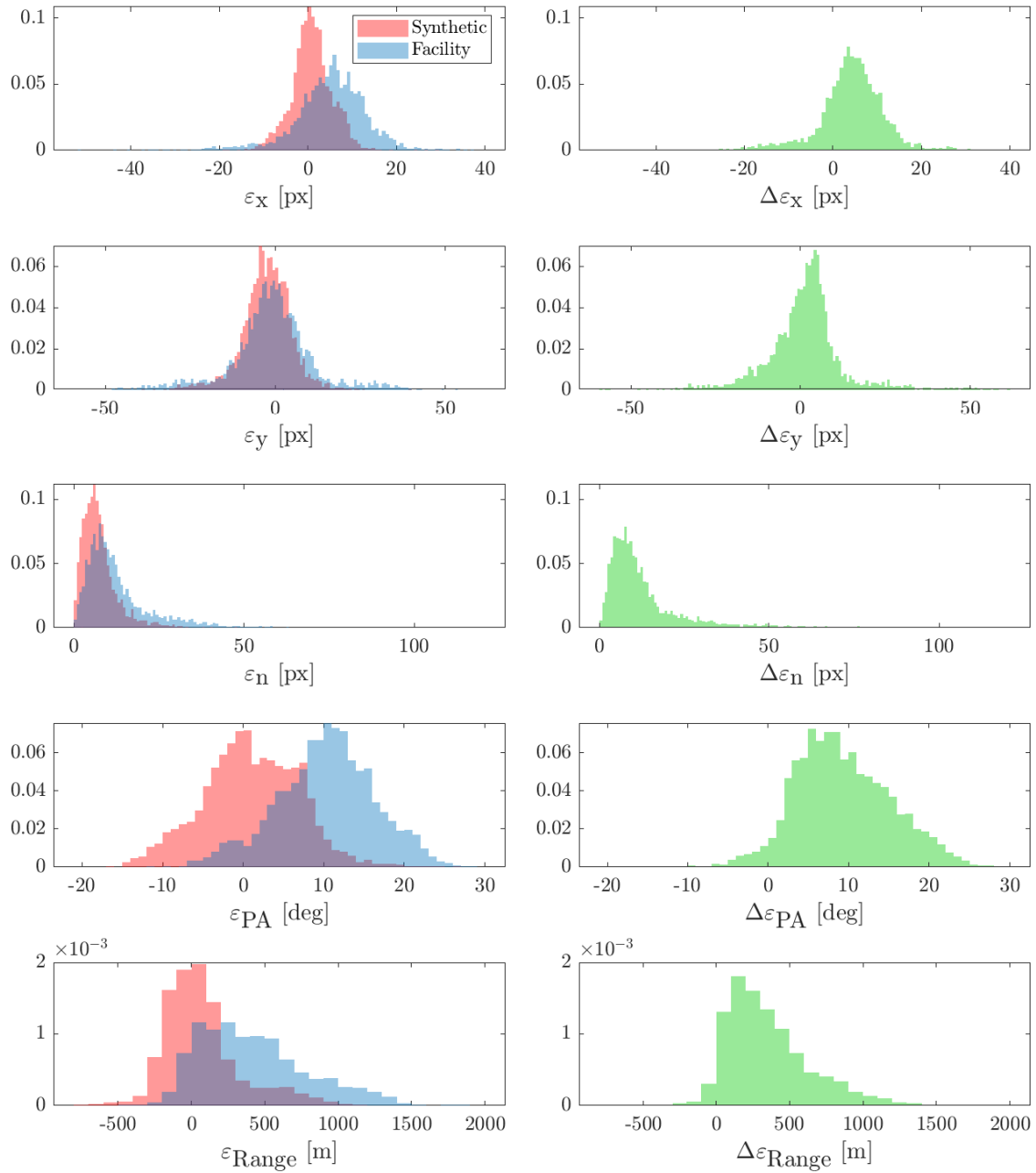
Figure 15: Results for the FRP dataset, shown as normalized histograms. Left: Estimation errors statistics. Right: Difference between the IP output on facility images and synthetic images.

Figure 16: Results for the CRP dataset, shown as normalized histograms. Left: Estimation errors statistics. Right: Difference between the IP output on facility images and synthetic images.

CONCLUSION

In this work the WCOB algorithm designed for the Milani mission is tested for the first time with hardware-in-the-loop images acquired employing the TinyV3RSE facility. The WCOB is tested in a wide variety of conditions by considering different geometrical configurations and hardware settings. The results show the robustness of the algorithm in all the considered test cases. Indeed, the algorithm is capable of providing good estimates of the CoF coordinates, even in challenging conditions. The PA and range estimates, instead, are more sensitive to hardware effects and have shown biased results. Nevertheless, they are of secondary interest, since they are just a byproduct of the CoF estimation procedure and they are not currently used for navigation purposes.

Future works could investigate the combined effect of exposure time and blur, which could cause a significant degradation in the performance. Furthermore, the effect of the IP algorithm on the GNC subsystem should be assessed in HIL closed loop simulations. Finally, the possibility to use TinyV3RSE-generated datasets to train the data-driven functions of the WCOB algorithm could be investigated. This would further advance the validation of the Milani's image processing towards realistic environmental conditions for flight operations. To conclude, this study is a preliminary but mandatory step toward the full validation and verification of the Milani IP pipeline.

ACKNOWLEDGMENTS

REFERENCES

[1] N. Rowell, S. Parkes, M. Dunstan, and O. Dubois-Matra, "PANGU: Virtual spacecraft image generation," *5th Int. Conf. on Astrodynamics Tools and Techniques, ICATT*, 2012.

[2] J. Lebreton, R. Brochard, M. Baudry, G. Jonniaux, A. H. Salah, K. Kanani, M. Le Goff, A. Masson, N. Ollagnier, P. Panicucci, A. Proag, and C. Robin, "Image Simulation for Space Applications with the SurRender Software," *Proceedings of the 11th International ESA Conference on Guidance, Navigation & Control Systems, 22 - 25 June 2021, Virtual*, 2021.

[3] G. Rufino and A. Moccia, "Laboratory test system for performance evaluation of advanced star sensors," *Journal of Guidance, Control, and Dynamics*, Vol. 25, No. 2, 2002, pp. 200–208.

[4] G. Rufino, D. Accardo, M. Grassi, G. Fasano, A. Renga, and U. Tancredi, "Real-time hardware-in-the-loop tests of star tracker algorithms," *International Journal of Aerospace Engineering*, Vol. 2013, 2013.

[5] C. Beierle and S. D'Amico, "Variable-magnification optical stimulator for training and validation of spaceborne vision-based navigation," *Journal of Spacecraft and Rockets*, Vol. 56, No. 4, 2019, pp. 1060–1072.

[6] B. Boone, J. Bruzzi, W. Dellinger, B. Kluga, and K. Strobehn, "Optical simulator and testbed for spacecraft star tracker development," *Optical Modeling and Performance Predictions II*, Vol. 5867, International Society for Optics and Photonics, 2005.

[7] R. Volpe, M. Sabatini, G. Palmerini, and D. Mora, "Testing and Validation of an Image-Based, Pose and Shape Reconstruction Algorithm for Didymos Mission," *Aerotecnica Missili & Spazio*, 2020, pp. 1–16.

[8] A. Petit, E. Marchand, and K. Kanani, "Vision-based space autonomous rendezvous: A case study," *2011 IEEE/RSJ International Conference on Intelligent Robots and Systems*, IEEE, 2011, pp. 619–624.

[9] J. Brannan, N. Scott, and C. Carignan, "Robot Servicer Interaction with a Satellite During Capture," *International Symposium on Artificial Intelligence, Robotics and Automation in Space (iSAIRAS)*, 2018.

[10] M. Zwick, I. Huertas, L. Gerdes, and G. Ortega, "ORGL–ESA'S test facility for approach and contact operations in orbital and planetary environments," 2018.

[11] G. D. Domenico, E. Andreis, A. C. Morelli, G. Merisio, V. Franzese, C. Giordano, A. Morselli, P. P. F. Ferrari, and F. Topputo, "Toward Self-Driving Interplanetary CubeSats: The ERC-funded project EX-TREMA," *72nd International Astronautical Congress 2021, 25-29 October 2021*, 2021.

[12] F. Ferrari, V. Franzese, M. Pugliatti, C. Giordano, and F. Topputo, "Preliminary mission profile of Hera's Milani CubeSat," *Advances in Space Research*, Vol. 67, No. 6, 2021, pp. 2010–2029, 10.1016/j.asr.2020.12.034.

[13] F. Topputo *et al.*, "Lunar Meteoroid Impact Observer (LUMIO): A CubeSat at Earth-Moon L2," *European Planetary Science Congress 2018*, Vol. 12, 2018.

[14] F. Topputo, Y. Wang, C. Giordano, V. Franzese, H. Goldberg, F. Perez-Lissi, and R. Walker, "Envelop of reachable asteroids by M-ARGO CubeSat," *Advances in Space Research*, Vol. 67, No. 12, 2021, pp. 4193–4221, 10.1016/j.asr.2021.02.031.

[15] P. Panicucci, M. Pugliatti, V. Franzese, and F. Topputo, "TinyV3RSE: The DART Vision-Based Navigation Test-bench," *AAS GN&C conference, 3 - 9 February 2022*, 2022.

[16] M. Pugliatti, V. Franzese, A. Rizza, F. Piccolo, C. Bottiglieri, C. Giordano, F. Ferrari, and F. Topputo, "Design of the on-board image processing of the Milani mission," *AAS GN&C conference, 3 - 9 February 2022*, 2022.

[17] P. Michel, M. Küppers, and I. Carnelli, "The Hera mission: European component of the ESA-NASA AIDA mission to a binary asteroid," *42nd COSPAR Scientific Assembly*, Vol. 42, 2018, pp. B1–1.

[18] M. Pugliatti, A. Rizza, F. Piccolo, V. Franzese, C. Bottiglieri, C. Giordano, F. Ferrari, and F. Topputo, "The Milani mission: overview and architecture of the optical-based GNC system," *Scitech 2022*, 2-7 Jan 2022. DOI: 10.2514/6.2022-2381.

[19] M. Pugliatti, V. Franzese, and F. Topputo, "Data-Driven Image Processing for Onboard Optical Navigation Around a Binary Asteroid," *Journal of Spacecraft and Rockets*, Jan. 2022. (Article in Advance), 10.2514/1.A35213.